

Pacman (II): Application and Testing

C. Vogt¹*, K. Dolag² and T. A. Enßlin¹

¹Max-Planck-Institut für Astrophysik, Karl-Schwarzschild-Str.1, Postfach 1317, 85741 Garching, Germany

²Dipartimento di Astronomia, Università di Padova, vicolo dell’Osservatorio 2, 35122 Padova, Italy

Accepted ??. Received ??.; in original form ???

ABSTRACT

We proposed a new method to calculate Faraday rotation measure (RM) maps from multi-frequency polarisation angle data (Dolag et al.) in order to avoid the so-called $n\pi$ -ambiguity. Here we apply our *Pacman* algorithm to two polarisation data sets of extended radio sources, Abell 2255 and Hydra A, and compare the RM maps obtained using *Pacman* to RM maps obtained employing already existing methods. We demonstrate the reliability and the robustness of *Pacman*. In order to study the influence of map making artefacts, which are imprinted by wrong solutions to the $n\pi$ -ambiguities, and of the error treatment of the data, we calculated and compared magnetic field power spectra from various RM maps. The power spectra were derived using the method recently proposed by Enßlin & Vogt (2003). We demonstrate the sensitivity of statistical analysis to artefacts and noise in the RM maps and thus, we demonstrate the importance of an unambiguous determination of RM maps and an understanding of the nature of the noise in the data. Additionally, we introduce and perform statistical tests to estimate the quality of the derived RM maps, which demonstrate the quality improvements due to *Pacman*.

Key words: Intergalactic medium – Galaxies: cluster: general

1 INTRODUCTION

Magnetic fields are ubiquitous throughout the universe. One method to study them is the analysis of the Faraday rotation effect. This effect describes that if polarised radiation traverses a magnetised plasma the plane of polarisation of the radiation is rotated. The change in polarisation angle is proportional to the squared wavelength λ^2 . The proportionality constant is called rotation measure (RM). Various methods have been proposed in order to calculate RM maps from multi-frequency polarisation data sets (e.g. Vallée & Kronberg 1975; Haves 1975; Ruzmaikin & Sokoloff 1979; Sarala & Jain 2001). The difficulty involved in this calculation arises from the fact that observations constrain the polarisation angle φ only up to additions of $\pm n\pi$. This leads to the so-called $n\pi$ -ambiguity.

In a previous paper (Dolag et al. 2003, hereafter Paper I), we proposed a new approach for the unambiguous determination of RM and of the intrinsic polarisation angle φ^0 at the observed, polarised radio source from multi-frequency polarisation data sets. The proposed algorithm uses a global scheme in order to solve the $n\pi$ -ambiguity. It assumes that if regions exhibit small polarisation angle gradients between neighbouring pixels in all observed frequencies simultaneously then these pixels can be considered as connected. Information about one pixel can be used for neighbour-

ing ones and especially the solution to the $n\pi$ -ambiguity should be the same.

Faraday rotation measure maps are analysed in order to get insight into the properties of the RM producing magnetic fields such as field strengths and correlation lengths. Artefacts in RM maps which result from $n\pi$ -ambiguities can lead to misinterpretation of the data. Recently, Enßlin & Vogt (2003) proposed a method to calculate magnetic power spectra from RM maps and to estimate magnetic field properties. They successfully applied their method to RM maps (Vogt & Enßlin 2003) and realised that map making artefacts and small scale pixel noise have a tremendous influence on the shape of the magnetic power spectra on large Fourier scales – small real space scales. Thus, for the application of these kind of statistical methods it is desirable to produce unambiguous RM maps with as little noise as possible. This and similar applications are our motivations for designing *Pacman* (Paper I) and to quantify its performance (this Paper).

In order to detect and to estimate the correlated noise level in RM and φ^0 maps, Enßlin et al. (2003) recently proposed a gradient vector product statistic. It compares RM gradients and intrinsic polarisation angle gradients and aims to detect correlated fluctuations on small scales, since RM and φ^0 are both derived from the same set of polarisation angle maps.

* E-mail: cvogt@mpa-garching.mpg.de (CV); kdolag@pd.astro.it (KD); ensslin@mpa-garching.mpg.de (TAE)

In Paper I, we describe in detail the idea and the implemen-

tation of the *Pacman*¹ algorithm. Here, we want to apply this algorithm to polarisation observation data sets of two extended polarised radio sources located in the Abell 2255 (Govoni et al. 2002) cluster and the Hydra cluster (Taylor & Perley 1993). This is described in Sect. 3. Using these polarisation data, we demonstrate the stability of our *Pacman* algorithm and compare RM maps obtained from a standard fit algorithm. A “standard fit” algorithm is considered to be the algorithm which performs a pixel by pixel least squares fit using the methods suggested by Vallée & Kronberg (1975); Haves (1975); Ruzmaikin & Sokoloff (1979).

We demonstrate the importance of the unambiguous determination of RMs for a statistical analysis by applying the statistical approach developed by Enßlin & Vogt (2003) to the RM maps in order to derive the power spectra and strength of the magnetic fields in the intra-cluster medium. We also discuss the influence of error treatment in the analysis. The philosophy of this statistical analysis and the calculation of the power spectra is briefly outlined in Sect. 2.1 whereas the results of the application to the RM maps are presented in Sect. 3.

In addition, we apply the *gradient vector product statistic* V as proposed by Enßlin et al. (2003) in order to detect map making artefacts and correlated noise. The concept of this statistic is briefly explained in Sect. 2.2 and in Sect. 3, it is applied to the data. After the discussion of our results, we give our conclusions and lessons learned from the data during the course of this work in Sect. 4.

Throughout the rest of the paper, we assume a Hubble constant of $H_0 = 70 \text{ km s}^{-1} \text{ Mpc}^{-1}$, $\Omega_m = 0.3$ and $\Omega_\Lambda = 0.7$ in a flat universe. The notation used follows Paper I.

2 STATISTICAL ANALYSIS OF RM MAPS

2.1 Magnetic Power Spectra

Our *Pacman* algorithm is especially useful for the determination of RM maps of extended radio sources. RM maps of extended radio sources are frequently analysed in terms of correlation length and the RM producing magnetic field strength. One analysis relying on statistical methods in order to derive magnetic field power spectra was recently developed by Enßlin & Vogt (2003). They successfully applied their method to existing RM maps of radio sources located in Abell 2634, Abell 400 and Hydra A (Vogt & Enßlin 2003). In the course of their work, they realised that their method is sensitive to map making artefacts and pixel noise, which can lead to misinterpretation of the data at hand. Therefore, their method, which we briefly describe below, is a good opportunity to show the importance of the reliable determination of RM maps.

Their method is based on the assumption that the magnetic fields causing the Faraday rotation measures are isotropically distributed throughout the Faraday screen. If the sampling volume of these fields is sufficiently large, the fields can be regarded as statistically isotropic and statistically homogeneous. Therefore, the statistical average over any field quantity will not depend on the geometry or the location of the sampling volume.

The Faraday rotation is related to the projected magnetic field distribution parallel to a line of sight

$$\text{RM}(\vec{x}_\perp) = a_0 \int_{z_s(\vec{x}_\perp)}^{\infty} dz n_e(\vec{x}) B_z(\vec{x}), \quad (1)$$

¹ The computer code for *Pacman* will be publicly available at <http://dipastro.pd.astro.it/~cosmo/Pacman>

where \vec{x}_\perp is the displacement of the line of sight from the z -axis, $z_s(\vec{x}_\perp)$ is the location of the source, $a_0 = e^3/(2\pi m_e^2 c^4)$, $\vec{x} = (\vec{x}_\perp, z)$, $n_e(\vec{x})$ is the electron density and $B_z(\vec{x})$ is the magnetic field component parallel to the line of sight.

An RM autocorrelation function and a magnetic field autocorrelation tensor can be introduced. Using the assumptions mentioned above and the divergence-freeness of magnetic fields, one can define the *scalar magnetic autocorrelation function* $w(r)$ as the trace of the magnetic field autocorrelation tensor. Using the relation between the observable RM and the magnetic field component along the line of sight expressed by Eq.(1), it is possible to establish an analytical relationship between RM and $w(r)$.

Interesting magnetic field quantities such as correlation length and central field strength can be determined from the magnetic autocorrelation function $w(r)$. Furthermore, the autocorrelation function is equivalent to the Fourier transform of the power spectrum as stated by the Wiener–Khinchin Theorem. Therefore, it is also possible to determine the one dimensional power spectrum of the magnetic field $\varepsilon_B(k)$.

The observational nature of the data are taken into account by introducing a window function, which can be interpreted as the sampling volume. The window function will be zero at points located outside the sampling volume which is situated in front of the radio source and thus, accounts for the limited source size. Additionally, the window function describes global properties of electron density and magnetic field distribution within the Faraday screen between source and observer.

In addition, a noise reducing data weighting scheme can be introduced to account for observational noise. One reasonable choice of weighting is to introduce a factor $\sigma_0^{\text{RM}}/\sigma_{ij}^{\text{RM}}$, which we call simple window weighting. Another possible weighting scheme is a thresholding scheme described by $1/(1 + \sigma_0^{\text{RM}}/\sigma_{ij}^{\text{RM}})$, which means that the noise below a certain threshold σ_0^{RM} is acceptable and areas of higher noise are down-weighted.

Note, that magnetic power spectra, which are calculated using the approach explained above, are used as valuable estimator for magnetic field strengths and correlation lengths. However, since the spectra are shaped by and are very sensitive to small scale noise and map making artefacts, we use them here to quantify the influence of noise and artefacts rather than as an estimator for characteristic properties of the RM producing field strengths.

2.2 Gradient Vector Product Statistic

Enßlin et al. (2003) introduced a *gradient vector product statistic* V to reveal correlated noise in the data. Observed RM and φ^0 maps will always have some correlated fluctuations on small scales, since they are both calculated from the same set of polarisation angle maps, leading to correlated fluctuation in both maps. The noise correlation between φ^0 and RM errors is an anti-correlation of linear shape and can be detected by comparing the gradients of these quantities. A suitable quantity to detect correlated noise between φ^0 and RM is therefore

$$V = \frac{\int d^2x \nabla \text{RM}(\mathbf{x}) \cdot \nabla \varphi^0(\mathbf{x})}{\int d^2x |\nabla \text{RM}(\mathbf{x})| |\nabla \varphi^0(\mathbf{x})|}, \quad (2)$$

where $\nabla \text{RM}(\mathbf{x})$ and $\nabla \varphi^0(\mathbf{x})$ are the gradients of RM and φ^0 . A map pair, which was constructed from a set of independent random polarisation angle maps $\varphi(k)$, will give a $V \gtrsim -1$. A map pair without any correlated noise will give a $V \approx 0$. Hence, the statistic V is suitable to detect especially correlated small scale pixel noise.

The denominator in Eq. (2) is the normalisation and enables the comparison of V for RM maps of different sources, since V is proportional to the fraction of gradients which are artefacts. Since, we especially want to compare the quality between maps of the same source calculated using the two different algorithms, it is useful to introduce the unnormalised quantity

$$\tilde{V} = \int d^2x \nabla \text{RM}(\mathbf{x}) \cdot \nabla \varphi^0(\mathbf{x}). \quad (3)$$

The quantity \tilde{V} gives the absolute measure of correlation between the gradient alignments of RM and φ^0 . The smaller this value is the smaller is the total level of correlated noise in the maps.

2.3 Error Under or Over Estimation

One problem, we were faced with during the course of our statistical analysis is the possibility that the measurement errors are under or overestimated. Such a hypothesis can be tested by calculating a measure of the deviation of the data points from the RM fits:

$$S^2 = \left\langle \frac{\Delta_{\text{obs},ij}^2(k)}{\sigma_{k,ij}^2} \right\rangle_{ijk}, \quad (4)$$

where $\langle \rangle_{ijk}$ means the map (sum over pixels (ij)) and frequency (sum over k 's) average and $\Delta_{\text{obs},ij}^2(k) = [\varphi_{\text{obs},ij}(k) - (\text{RM}_{ij} \lambda_k^2 + \varphi_{ij}^0)]^2$ is the actual deviation of the measured $\varphi_{\text{obs},ij}(k)$ from the value calculated using the results of the least-squares fit. If this value is equal to unity then the errors are neither under nor overestimated. For a $S^2 > 1$, the errors have been underestimated and for a $S^2 < 1$, they have been overestimated. Unfortunately this analysis does not reveal in its simple form at which frequency the errors might be under or overestimated.

One can compare the value derived from the actual polarisation data with the theoretically calculated value, which can be defined by

$$S_k^2 = \frac{\langle \Delta_k^2 \rangle}{\sigma_k^2} = \frac{\langle (\varphi(k)_{\text{obs}} - \varphi(k)_{\text{corr}})^2 \rangle}{\sigma_k^2}, \quad (5)$$

where $\varphi(k)_{\text{corr}} = \text{RM}^{\text{obs}} \lambda_k^2 + \varphi_{\text{obs}}^0$. In the latter expression, φ_{obs}^0 and RM^{obs} depend on the measured polarisation angle $\varphi_{\text{obs}}(k)$ through the least-squares fit equation used for their determination.

Introducing a $\delta\varphi_k = \varphi_{\text{obs}}(k) - \varphi(k)$, which is the difference between observed and true polarisation angle and assuming the same noise levels for all frequencies, i.e. $\sigma_k = \sigma$ and $\delta_k = \delta$, then Eq. (5) can be expressed with the help of Eq. (3) and (4) of Paper I by

$$\frac{\langle \Delta_k^2 \rangle}{\sigma_k^2} = \left(1 - \frac{\lambda_k^4 \bar{S} - 2\lambda_k^2 \bar{\lambda}^2 + \bar{\lambda}^4}{\sigma^2 (\bar{\lambda}^4 \bar{S} - \bar{\lambda}^2)^2} \right) \frac{\langle \delta\varphi^2 \rangle}{\sigma^2}, \quad (6)$$

where $\bar{S} = \sum_{k=1}^f 1/\sigma_k^2$, $\bar{\lambda}^4 = \sum_{k=1}^f \lambda_k^4/\sigma_k^2$ and $\bar{\lambda}^2 = \sum_{k=1}^f \lambda_k^2/\sigma_k^2$. The factor $(1-...)$ describes the turn of the fitted lines in the individual fits of RM due to the influence of the measurement errors σ_k .

Averaging over the $k = 1 \dots f$ frequencies yields

$$S^2 = \sum_k \frac{1}{f} \frac{\langle \Delta_k^2 \rangle}{\sigma_k^2} = \left(1 - \frac{2}{f} \right) \frac{\langle \delta\varphi^2 \rangle}{\sigma^2}. \quad (7)$$

Thus, for a large number of observed frequencies f , the value of $2/f$ becomes negligible in the equation above and the measured S^2 is a true measure for the under or over estimation of the measurement errors. However, for a definite number of frequencies f , this factor leads to a decrease in the actual measured S^2 , where the true measure of the under estimation of errors $\tilde{S} = \langle \delta\varphi^2 \rangle / \sigma^2$ is larger by a factor of $f / (f - 2)$.

3 APPLICATION TO DATA

For the calculation of what we call further on the standard fit RM maps, we used the χ^2 method suggested by Vallée & Kronberg (1975) and Haves (1975). Also for the individual RM fits, we adopted this method. We used as an upper limit for the RM values $|\text{RM}|_{ij} = \text{RM}^{\text{max}} \pm 3\sigma_{ij}^{\text{RM}}$, where σ_{ij}^{RM} was calculated following Eq.(5) in Paper I. The least-squares fit for the individual data points were always performed as error weighted fits as described by Eq. (3) and (4) in Paper I, if not stated otherwise. For the *Pacman* calculations, we used for the free parameters $\alpha = \beta = 1$ in Eq. (7) in Paper I.

However, we also used the method suggested by Ruzmaikin & Sokoloff (1979) as standard fit algorithm. The results did not change substantially.

3.1 Abell 2255E

The Abell cluster 2255, which has a redshift of 0.0806 (Struble & Rood 1999), has been studied by Burns et al. (1995) and Feretti et al. (1997). The polarised radio source B1713+641, which we call hereafter A2255E, has a two sided radio lobe structure and is not directly located in the cluster centre. Polarisation observations were performed using the Very Large Array (VLA) at 4535, 4885, 8085, and 8465 MHz. The data reduction was done with standard AIPS (Astronomical Imaging Processing Software) routines (Govoni et al., in prep.). The polarisation angle maps and their standard error maps for the four frequencies were kindly provided to us by Federica Govoni. A preliminary analysis of an RM map of this source in order to determine the properties of the magnetic field in the intra-cluster gas in Abell 2255 is presented in Govoni et al. (2002).

Using the polarisation angle data, an RM map employing the standard fit algorithm was calculated, where the maximal allowed error in polarisation angle was chosen to be $\sigma_k^{\text{max}} = 25^\circ$. The resulting RM map is shown in the upper left panel of Fig 1. The overlaid contour indicates the area which would be covered if polarisation angle errors are limited by $\sigma_k^{\text{max}} = 10^\circ$. For these calculations, we assumed $\text{RM}^{\text{max}} = 1500 \text{ rad m}^{-2}$.

As can be seen from this map, typical RM values range between -100 rad m^{-2} and $+210 \text{ rad m}^{-2}$. Since this cluster is not known to inhabit a cooling core in its centre (Feretti et al. 1997), these are expected values. However, the occurrence of RM values around 1000 rad m^{-2} , which can be seen as grey areas in the standard fit map of A2255E, might indicate that for these areas the $n\pi$ -ambiguity was not properly solved. One reason for this suspicion is found in the rapid change of RM values occurring between 1 or 2 pixel from 100 to 1000 rad m^{-2} . All these jumps have a ΔRM of about 1000 rad m^{-2} indicating $n\pi$ -ambiguities between 4 GHz and 8 GHz which can be theoretically calculated from $\Delta\text{RM} = \pi / (\lambda_2^2 - \lambda_1^2)$. Another important point to note is that parts of the grey areas lie well within the $\sigma_k^{\text{max}} = 10^\circ$ contour, and hence, contribute to the results of any statistical analysis of such a parametrised RM map.

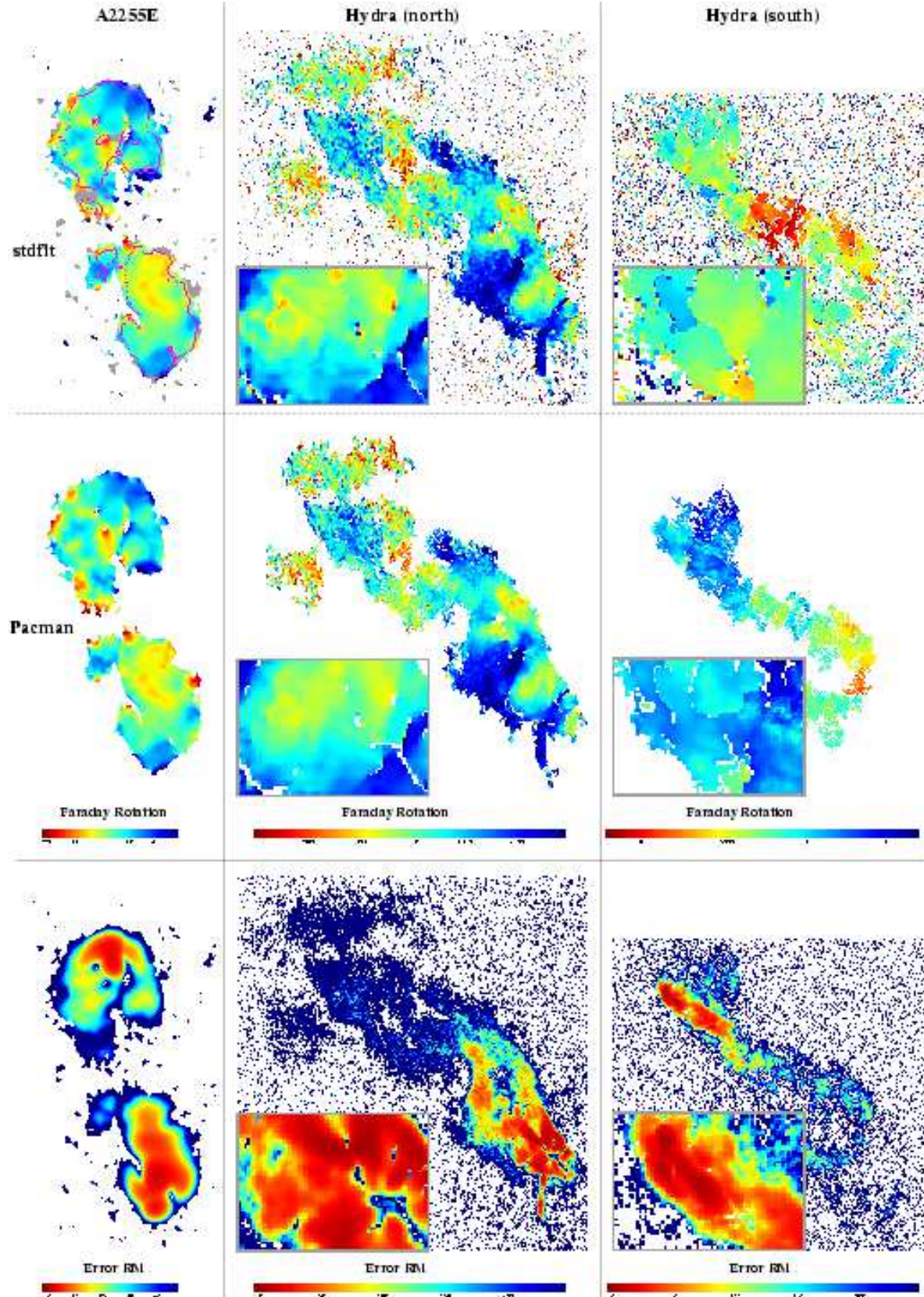


Figure 1. Comparison of the standard fit RM maps (upper panels) and the *Pacman* RM maps (middle panels) for A2255E (left column), the north (middle column) and the south lobe (right column) of Hydra A. RM values not represented by the colour bar are coloured in grey. Panels at the bottom exhibit the respective σ_k^{RM} -maps. For the standard fit RM map of A2255E a $\sigma_k^{\text{max}} = 25^\circ$ and $k_{\min} = f = 4$ was used, contours indicate the area covered by a standard fit RM map with $\sigma_k^{\text{max}} = 10^\circ$. The parameters used for the *Pacman* RM map of A2255E are $\sigma_k^{\text{max}} = 25^\circ$, $\sigma_k^{\Delta} = 25^\circ$, $g = 1.2$ and $k_{\min} = f = 4$; for the standard fit RM maps of Hydra A are $\sigma_k^{\text{max}} = 25^\circ$ and $k_{\min} = f = 4$ (at 8 GHz); for the *Pacman* RM map of Hydra (north) are $\sigma_k^{\text{max}} = 30^\circ$, $k_{\min} = 4$, $f = 5$, $\sigma_k^{\Delta} = 25^\circ$ and $g = 1.5$; for the *Pacman* RM map of Hydra (south) are $\sigma_k^{\text{max}} = 35^\circ$, $k_{\min} = f = 5$, $\sigma_k^{\Delta} = 35^\circ$ and $g = 2.0$.

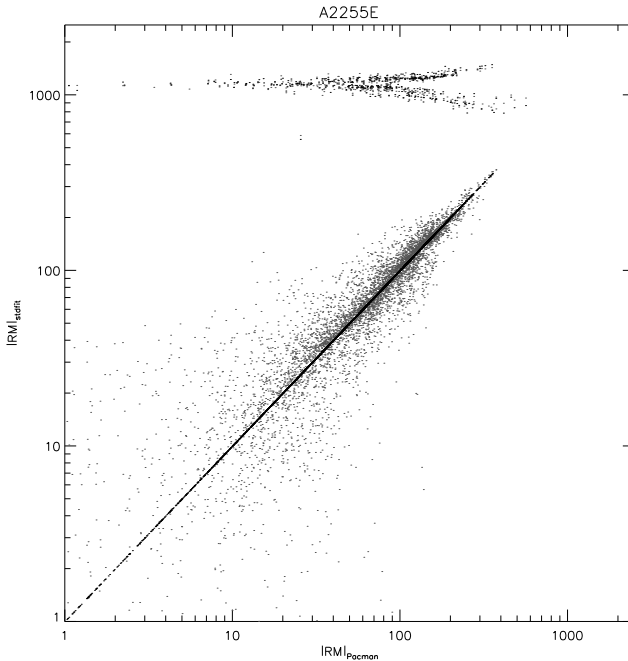


Figure 2. A pixel-by-pixel scatter plot of $|\text{RM}|_{\text{stdfit}}$ values obtained using the standard fit on the y -axis versus the $|\text{RM}|_{\text{Pacman}}$ values calculated by employing our new algorithm *Pacman*. Black points represent results from an error weighted standard least-squares fit and grey points from a non-error weighted standard fit. The horizontal line developing at $|\text{RM}|_{\text{stdfit}}$ values of around 1000 rad m^{-2} are artefacts of a wrong solution of the $n\pi$ -ambiguity.

Therefore, the polarisation data of this source provide a good possibility to demonstrate the robustness and the reliability of our proposed algorithm. The RM map calculated by *Pacman* is shown in the middle left panel. The same numbers for the corresponding parameters were used; $\sigma_k^{\max} = 25^\circ$, $\text{RM}^{\max} = 1500 \text{ rad m}^{-2}$.

An initial comparison by eye reveals that the method used in the standard fit procedure produces spurious RMs in noisy regions (manifested as grey areas in the upper left panel of Fig. 1) as previously mentioned while the RM map calculated by *Pacman* shows no such grey areas. The apparent jumps of about 1000 rad m^{-2} observed in the standard fit map have disappeared in the *Pacman* map.

A pixel-by-pixel comparison is shown in Fig. 2. In this figure the $|\text{RM}|_{\text{stdfit}}$ values obtained for pixels using a standard fit are plotted on the y -axis against the $|\text{RM}|_{\text{Pacman}}$ values obtained at the same corresponding pixel locations using the *Pacman* algorithm on the x -axis. The black points represent the error weighted standard fit whereas the grey points represent the non-error weighted standard fit. Note that *Pacman* applied only an error weighted least-squares fit to the data. From this scatter plot, one can clearly see that both methods yield same RM values for most of the points which is expected from the visual comparison of both maps. However, the horizontal line developing for $|\text{RM}|_{\text{stdfit}}$ values at around 1000 rad m^{-2} are due to the wrong solution of the $n\pi$ -ambiguity found by the standard fit algorithm. The splitting develops because we plotted absolute values $|\text{RM}|$ rather than differences.

For the demonstration of the effect of $n\pi$ -ambiguity artefacts and pixel noise on statistical analysis, we determined the cluster magnetic field power spectra by employing the approach briefly described in Sect. 2.1. For detailed discussion and description of the application of the method to data, we refer the reader to Vogt &

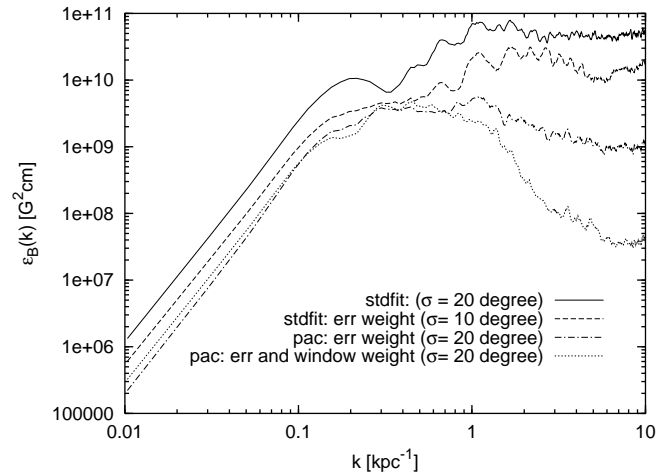


Figure 3. Various power spectra for the cluster Abell 2255 determined from different RM map making scenarios are shown. The solid line represents a power spectrum calculated from a standard fit RM map with $\sigma_k^{\max} = 20^\circ$ where no error weighting was applied. The dashed power spectrum was obtained from a standard fit RM map with $\sigma_k^{\max} = 10^\circ$ where error weighting was applied to the standard fit. The dashed-dotted power spectrum was determined from a *Pacman* RM map with $\sigma_k^{\max} = 20^\circ$ and error weighting was applied to the RM fits. The dotted line represents a power spectrum calculated from a *Pacman* RM map as above, but additionally a simple window weighting was applied for the determination of the power spectra.

Enßlin (2003). In the calculation, we assumed that the source plane is parallel to the observer plane. Please note, that the application of an RM data filter in order to remove bad data or data which might suffer from a wrong solution to the $n\pi$ -ambiguity as described by Vogt & Enßlin (2003) is here not necessary and not desirable. This is on the one hand due to the use of an error weighting scheme in the window function to suppress bad data and on the other hand due to the wish to study the influence of noise and map making artefacts on the power spectra.

The RM area used for the calculation of any power spectrum is the RM area which would be covered by the *Pacman* algorithm while using the same set of parameter σ_k^{\max} , RM^{\max} . This ensures that pixels on the border or noisy regions of the image not associated with the source – as seen in the standard fit RM map of A2255E in the upper left panel of Fig. 1 – are not considered for the analysis. (The same philosophy also applies for the discussion of the Hydra data in Sect. 3.2 and Sect. 3.3).

The power spectra calculated for various map making scenarios are shown in Fig. 3. The solid and dashed line represent power spectra calculated from standard fit RM maps. The solid line was calculated from an RM map which was obtained by using $\sigma_k^{\max} = 20^\circ$ where no error weighting was applied to the standard fit. The possible window weighting as mentioned in the end of Sect. 2.1 was also not applied. This scenario is therefore considered as a worst case. The dashed line was calculated from an RM map employing an error weighted standard fit while only allowing errors in the polarisation angle of $\sigma_k^{\max} = 10^\circ$. Again no window weighting was applied. From the comparison of these two power spectra alone, one can see that the large k -scales – and thus small real space scales – are sensitive to pixel-noise. Therefore, the application of an error weighted least square fit in the RM calculation leads to a reduction of noise in the power spectra. Note that in these two power spectra, the influence of the $n\pi$ -artefacts are still present even in the error weighted standard fit RM map.

The two remaining power spectra in Fig. 3 allow us to investigate the influence of the $n\pi$ -artefacts. The dashed-dotted line represents the power spectra as calculated from a *Pacman* RM map allowing $\sigma_k^{\max} = 20^\circ$ performing an error weighted fit. Again, no window weighting was applied to this calculation. One can clearly see that there is one order of magnitude difference between the error weighted standard fit power spectra and the *Pacman* one at large k -values. Since we also allow higher noise levels σ_k^{\max} for the polarisation angles, this drop can only be explained by the removing of the $n\pi$ -artefacts in the *Pacman* map. That there is still a lot of noise in the map on small real space scales (large k 's), which governs the power spectra on these scales, can be seen from the dotted power spectrum, which was determined as above while applying a simple window weighting in the calculation. There is an additional difference of about one order of magnitude between the two power spectra at large k -scales determined for the two *Pacman* scenarios.

As another independent statistical test, we applied the *gradient vector alignment statistic* \tilde{V} to the RM and φ^0 maps calculated by the *Pacman* and the standard fit algorithm. The gradients of RM and φ^0 were calculated using the scheme as described in footnote 5 in Enßlin et al. (2003). For the two RM maps shown in Fig. 1, we find a ratio of $\tilde{V}_{\text{stdfit}}/\tilde{V}_{\text{pacman}} = 20$, which indicates a significant improvement mostly resulting from removing the $n\pi$ -artefacts by the *Pacman* algorithm. The calculation of the normalised quantity V yielded $V_{\text{stdfit}} = -0.75$ and $V_{\text{pacman}} = -0.87$. Smoothing the *Pacman* RM map slightly leads to a drastic decrease of the quantities \tilde{V} and V . This indicates that the statistic is still governed by small scale noise. This can be understood by looking at the RM maps of Abell 2255 in Fig. 1. The extreme RM values are situated at the margin of the source which is, however, also the noisiest region of the source. Calculating the normalised quantity for the high signal-to-noise region yields $V_{\text{pacman}} = -0.47$.

3.2 Hydra North

The polarised radio source Hydra A, which is in the centre of the Abell cluster 780, also known as the Hydra A cluster, is located at a redshift of 0.0538 (de Vaucouleurs et al. 1991). The source Hydra A shows an extended, two-sided radio lobe. Detailed X-ray studies have been performed on this cluster (e.g. Ikebe et al. 1997; Peres et al. 1998; David et al. 2001). They revealed a strong cooling core in the cluster centre. The Faraday rotation structure was observed and analysed by Taylor & Perley (1993). They reported RM values ranging between $-1\,000 \text{ rad m}^{-2}$ and $+3\,300 \text{ rad m}^{-2}$ in the north lobe and values down to $-12\,000 \text{ rad m}^{-2}$ in the south lobe.

Polarisation angle maps and their error maps for frequencies at 7 815, 8 051, 8 165, 8 885 and 14 915 MHz resulting from observation with the Very Large Array were kindly provided to us by Greg Taylor. A detailed description of the radio data reduction can be found in Taylor et al. (1990) and Taylor & Perley (1993).

In this section, we concentrate on the north lobe of Hydra A and discuss the south lobe separately in Sect. 3.3. The south lobe is more depolarised, leading to a lower signal-to-noise than in the north lobe. The north lobe is a good example of how to treat noise in the data, while the south lobe gives a good opportunity to discuss the limitations and the strength of our algorithm *Pacman*.

Using the polarisation data for the four frequencies at around 8 GHz, we calculated the standard fit RM map which is shown in the upper middle panel of Fig. 1. The maximal allowed error in polarisation angle was chosen to be $\sigma_k^{\max} = 25^\circ$ and $\text{RM}^{\max} = 15\,000 \text{ rad m}^{-2}$. A *Pacman* RM map is shown in the middle of the middle panel in Fig. 1 below the standard fit map.

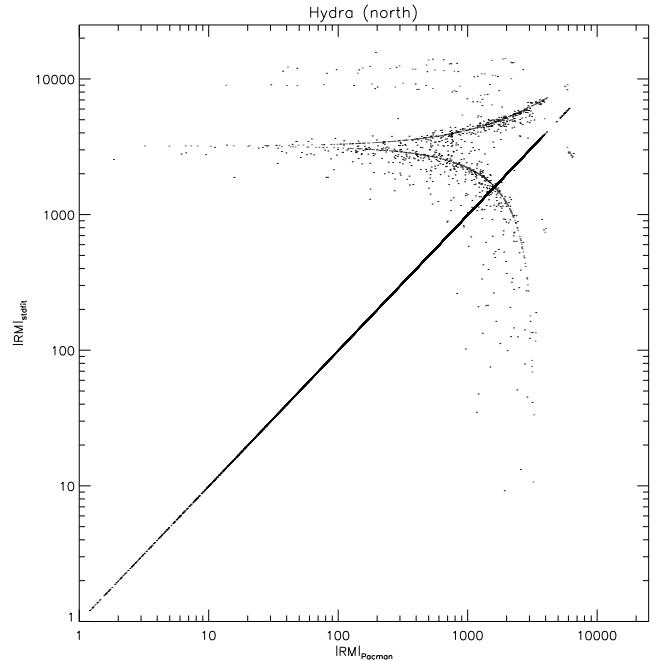


Figure 4. A pixel-by-pixel comparison for the Hydra north lobe of $|\text{RM}|_{\text{stdfit}}$ values obtained using the standard fit plotted on the y -axis versus the $|\text{RM}|_{\text{Pacman}}$ values calculated by employing our new algorithm *Pacman*. The two horizontal branches developing are a result of spurious solution to the $n\pi$ -ambiguity obtained by the standard fit algorithm. For the calculation of the RM maps, all five frequencies were used.

This map was calculated using the four frequencies at around 8 GHz with a $\sigma_{k=8\text{GHz}}^{\max} = 30^\circ$ and additionally where possible the fifth frequency at 15 GHz was used with a $\sigma_{k=15\text{GHz}}^{\max} = 35^\circ$. RM^{\max} was chosen to be $15\,000 \text{ rad m}^{-2}$. From a visual comparison of the two maps, one can conclude that the standard fit map looks more structured on smaller scales and less smooth than the *Pacman* map. This structure on small scales might be misinterpreted as small scale structure of the RM producing magnetic field. Note that the difference in the RM maps is mainly due to the usage of the fifth frequency for the *Pacman* map demonstrating that all information available should be used for the calculation of RM maps in order to avoid misinterpretation of the data.

Since the four frequencies around 8 GHz are close together, a wrong solution of the $n\pi$ -ambiguity would manifest itself by differences of about $\Delta\text{RM} = 10\,000 \text{ rad m}^{-2}$. Such jumps are not observed in the main patches of the standard fit RM map shown in Fig. 1. However, including the information contained in the polarisation angle map of the 5th frequency at 15 GHz, which is desirable as explained above, one introduces the possibility of $n\pi$ -ambiguities resulting in $\Delta\text{RM} = 3\,000\ldots4\,000 \text{ rad m}^{-2}$. Therefore, a scatter plot of a pixel-by-pixel comparison between a standard fit and a *Pacman* map, calculated both using the additional available information on the fifth frequency, is shown in Fig. 4. The horizontal branches are spurious solution found by the standard fit algorithm. The bend develops because we plotted absolute values $|\text{RM}|$ rather than differences.

In order to study the influence of the noise on small scales, we calculated the power spectra from RM maps obtained using different parameter sets for the *Pacman* and the standard fit algorithm. As for Abell 2255E, all calculations of power spectra were done for RM areas which would be covered by the *Pacman* fit if the same

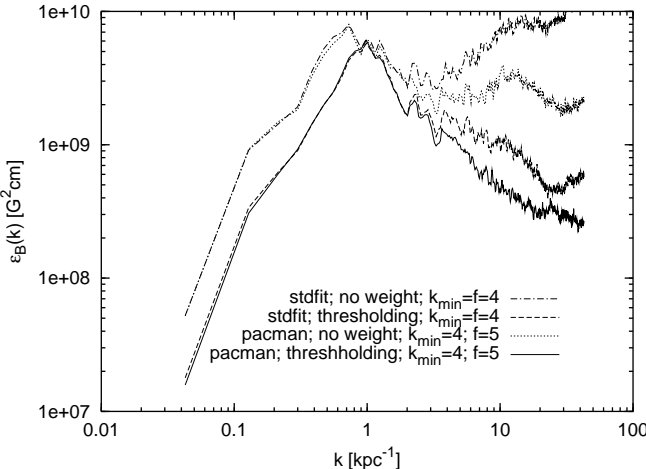


Figure 5. Various power spectra calculated for the RM maps for the north lobe of Hydra A are shown. The dashed dotted line and the dotted line represent the power spectra calculated from the standard fit RM map and the *Pacman* RM map, respectively, while no window weighting was applied. A threshold window weighting assuming a $\sigma_0^{\text{RM}} = 75 \text{ rad m}^{-2}$ yield the dashed line power spectrum for the standard fit map and the solid line for the *Pacman* map. The standard fit maps were calculated from the four frequencies at 8 GHz whereas the *Pacman* maps were determined using additionally the fifth frequency when possible. For both algorithms, $\sigma_k^{\text{max}} = 35^\circ$ was used. The influence of the small-scale pixel noise on the power spectra can clearly be seen in this figure at large k -values.

parameters were used. Again this leads to exclusion of pixels in the standard fit RM map which are not associated with the source.

There is a clear depolarisation asymmetry of the two lobes of Hydra A observed as described by the Laing–Garrington effect (Taylor & Perley 1993; Lane et al. 2003). Therefore, we assume for the calculation of any power spectra for the Hydra source, that the source plane is tilted by an inclination angle of 45° where the north lobe points towards the observer and the south lobe away from the observer.

For a first comparison, we calculated the power spectra for two RM maps similar to the one shown in Fig. 1. They were obtained using the four frequencies at 8 GHz for the standard fit algorithm and using additionally the fifth frequency when possible for the *Pacman* algorithm. The other parameters were chosen to be $\sigma_k^{\text{max}} = 35^\circ$ and $\text{RM}^{\text{max}} = 15000 \text{ rad m}^{-2}$. For these two RM maps, we determined power spectra applying firstly no window weighting at all and secondly threshold window weighting as described in the end of Sec. 2.1. We choose the threshold to be $\sigma_0^{\text{RM}} = 75 \text{ rad m}^{-2}$ which represents the high signal-to-noise region. The respective spectra are exhibited in Fig. 5.

For the power spectra, $n\pi$ -artefacts should play only a minor role in the calculation of the power spectra as explained above. Therefore, any differences arising in these spectra are caused by the varying treatment of noise in the map making process or in the analysis. Comparing the power spectra without window weighting, the one obtained from the *Pacman* RM map lies below the one from the standard fit RM map. The difference is of the order of half a magnitude for large k 's – small real space scales. The standard fit power spectrum seems to increase with larger k but the *Pacman* one seems to decrease over a greater range in k . The reason for this difference is the same one which was responsible for the different smoothness in the two RM maps shown in Fig. 1, namely that only four frequencies were used for the standard fit RM map. Even introducing

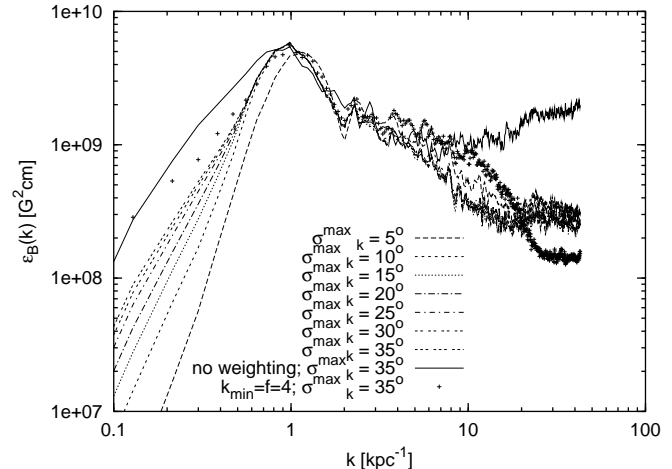


Figure 6. Power spectra for the north lobe of Hydra A calculated from a series of *Pacman* RM maps are shown. The various dashed and dotted lines show power spectra from RM maps calculated for σ_k^{max} ranging from 5° to 35° using all five frequencies $k_{\text{min}} = 5$. The spectra were determined applying threshold window weighting ($\sigma_0^{\text{RM}} = 50 \text{ rad m}^{-2}$). For comparison the solid line power spectrum, which is the largest spectrum at $k > 10 \text{ kpc}^{-1}$, is not window weighted for $\sigma_k^{\text{max}} = 35^\circ$. The power spectrum represented by the crosses was derived from an *Pacman* RM map obtained using the four frequencies at 8 GHz and a $\sigma_k^{\text{max}} = 35^\circ$.

a window weighting scheme, which down-weights noisy region, cannot account entirely for that difference as can be seen from the comparison of the window weighted power spectra. This is especially true because the small-scale spatial structures are found even in the high signal-to-noise regions when using only four frequencies for the RM map calculation. This demonstrates again how important it is to include all available information in the map making process.

In order to study the influence of the maximal allowed measurement error in the polarisation angle σ_k^{max} , we calculated the power spectra for a series of *Pacman* RM maps obtained for σ_k^{max} ranging from 5° to 35° . The RM maps were derived using all five frequencies $k_{\text{min}} = 5$, not allowing any points to be considered for which only four frequencies fulfil $\sigma_{k_{ij}} < \sigma_k^{\text{max}}$. Again an $\text{RM}^{\text{max}} = 15000 \text{ rad m}^{-2}$ was used. The resulting power spectra using a threshold window weighting ($\sigma_0^{\text{RM}} = 50 \text{ rad m}^{-2}$) are exhibited in Fig. 6. One can see that they are stable and do not differ substantially from each other even though the noise level increases slightly when increasing the σ_k^{max} . This demonstrates the robustness of our *Pacman* algorithm.

For comparison, we plotted two more power spectra in Fig. 6. For the solid line spectrum, no window weighting was applied to an RM map which was calculated as above having $\sigma_k^{\text{max}} = 35^\circ$. One can clearly see that the spectrum is governed by noise on large k -scales – small real space scales. Thus, some form of window weighting in the calculation of the power spectra seems to be necessary in order to suppress a large amount of noise.

Another aspect arises in the noise treatment if we consider the power spectra represented by the crosses which was calculated using a threshold window weighting ($\sigma_0 = 50 \text{ rad m}^{-2}$). This power spectrum represents the analysis for an RM map obtained using only the four frequencies at 8 GHz while $\sigma_k^{\text{max}} = 35^\circ$. It is striking that the noise level on large k -scales (on small real space scales) is lower than for the RM maps obtained for the five frequencies, one would expect it to be the other way round. Apparently the fifth fre-

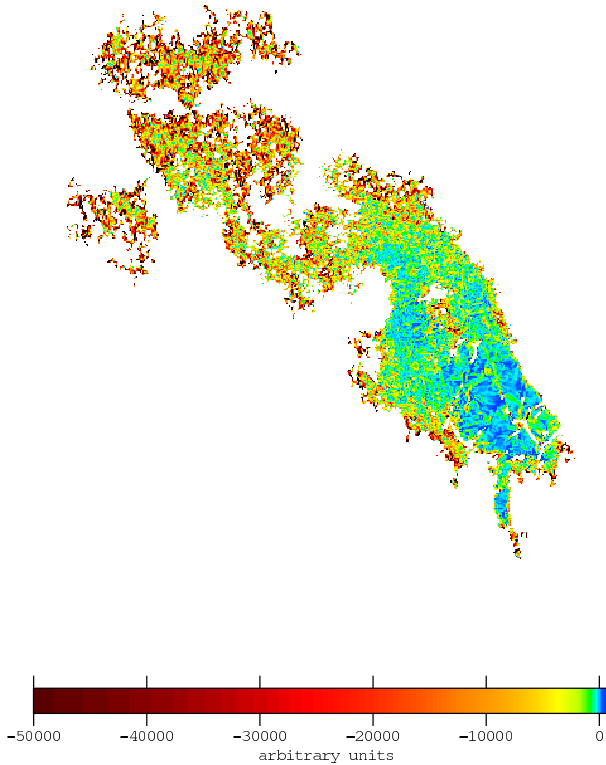


Figure 7. A \tilde{V} map for the north lobe of Hydra A is exhibited. The extreme negative values (red and black) correspond to strong anti-correlation of RM and φ^0 fluctuations, which are produced by noise in the observed maps. However, the green and blue coloured regions have values around zero and are therefore high signal-to-noise regions (compare with the σ_{ij}^{RM} map in the middle panel of Fig. 1).

frequency has a lot of weight in the determination of σ_{ij}^{RM} (see Eq. (3) in paper I) since this frequency is almost twice as large as the other four. If the measurement errors of the polarisation angles are underestimated this can lead to an underestimation of the uncertainty σ_{ij}^{RM} in the final RM value due to Gaussian error propagation.

One can test the hypothesis of underestimation of errors by calculating a S^2 as introduced in Sect. 2.3. Determining S^2 for the *Pacman* RM maps derived for four and for five frequencies yields a $S = 3$ for both cases. Following Eq. (7) and setting $f = 4$, the true measure of the underestimation of the measurement errors $\langle \delta\varphi^2 \rangle / \sigma^2$ becomes 18. This indicates that the standard errors in polarisation angles are underestimated by a factor of 4 on average and probably by a larger factor for the 5th frequency.

We also applied the gradient vector product statistic \tilde{V} to the RM and φ^0 maps obtained by using the RM maps as shown in the middle panel of Fig. 1 and the respective φ^0 maps. The calculation yielded for the ratio $\tilde{V}_{\text{stdfit}} / \tilde{V}_{\text{pacman}} = 1.2$. This corresponds to a slight decrease of correlated noise in the *Pacman* maps. The calculation of the normalised quantity resulted in $V_{\text{stdfit}} = -0.85$ for the standard fit and $V_{\text{pacman}} = -0.83$ for the *Pacman* maps. This is expected since the low signal-to-noise areas of the north lobe of Hydra A will govern this gradient statistic and for both RM maps these areas look very similar. In order to visualise this, we calculated a \tilde{V} map which is exhibited in Fig. 7. The extreme negative values observed for the low signal-to-noise regions (red regions) in-

dicate strong anti-correlation and thus, anti-correlated fluctuations of RM and φ^0 in these regions. For the high signal-to-noise regions (blue and green) moderate values varying around zero are observed. Note the striking morphological similarity of the RM error (σ^{RM}) map in the lower middle panel of Fig. 1 and of the \tilde{V} map as shown in Fig. 7. These two independent approaches to measure the RM maps accuracy give basically identical results. These approaches are complementary since they use independent information. The RM error map is calculated solely from σ_k maps, which are based on the absolute polarisation values, whereas the \tilde{V} map is based solely on the polarisation angle $\varphi(k)$ maps.

However, we note that the results for magnetic field strengths and correlation lengths presented by Vogt & Enßlin (2003) are not changed substantially. This is owing to the fact that Vogt & Enßlin (2003) considered for the calculation of the magnetic field properties only the power on scales which were larger than the resolution element (beam). Therefore the small scale noise was not considered for this calculation and thus, no change in the results given is expected. The central magnetic field strength for this cluster as derived during the course of this work is about 10 μG and the field correlation length is about 1 kpc being consistent with results presented in Vogt & Enßlin (2003).

3.3 The Quest for Hydra South

As already mentioned, the southern part of the Hydra source has to be addressed separately, as it differs from the northern part in many respects. One of them is that the depolarisation is higher in the south lobe which especially complicates the analysis of this part.

An RM map obtained employing the standard fit algorithm using the four frequencies at 8 GHz is shown in the upper right panel of Fig. 1. This RM map exhibits many jumps in the RM distribution which seems to be split in lots of small patches having similar RMs. Furthermore, RMs of $-12\,000 \text{ rad m}^{-2}$ are detected (indicated as red regions in the map). If one includes the fifth frequency at 15 GHz in the standard fit algorithm, the appearance of the RM map does not change significantly, and most importantly, the extreme values of about $-12\,000 \text{ rad m}^{-2}$ do not vanish.

The application of the *Pacman* algorithm with conservative settings for the parameters σ_k^{max} , σ_{\max}^{Δ} and g , leads to a splitting of the RM distribution into many small, spatially disconnected patches. Such a map does look like a standard fit RM map and there are still the RM jumps and the extreme RM values present. However, if one lowers the restrictions for the construction of patches, the *Pacman* algorithm starts to connect patches to the patch with the best quality data available in the south lobe using its information on the global solution of the $n\pi$ -ambiguity. An RM map obtained pushing *Pacman* to such limits is exhibited in the middle right panel of Fig. 1. Note that the best quality area is covered by the bright blue regions and a zoom-in for this region is also exhibited in the small box to the lower left of the source. In the lowest right panel of Fig. 1, a σ^{RM} -map is shown indicating the high quality regions by the red colour.

The RM distribution in this *Pacman* map exhibits clearly fewer jumps than the standard fit map although the jumps do not vanish entirely. Another feature that almost vanishes in the *Pacman* map are the extreme RMs of about $-12\,000 \text{ rad m}^{-2}$. The RM distribution of the *Pacman* map seems to be smoother than the one of the standard fit map. However, if the individual RM fits for points, which deviate in their RM values depending on the algorithm used, are compared in a $\varphi(k)$ - λ_k^2 -diagram, the standard fit seems to be the one which would have to be preferred since it does fit better to

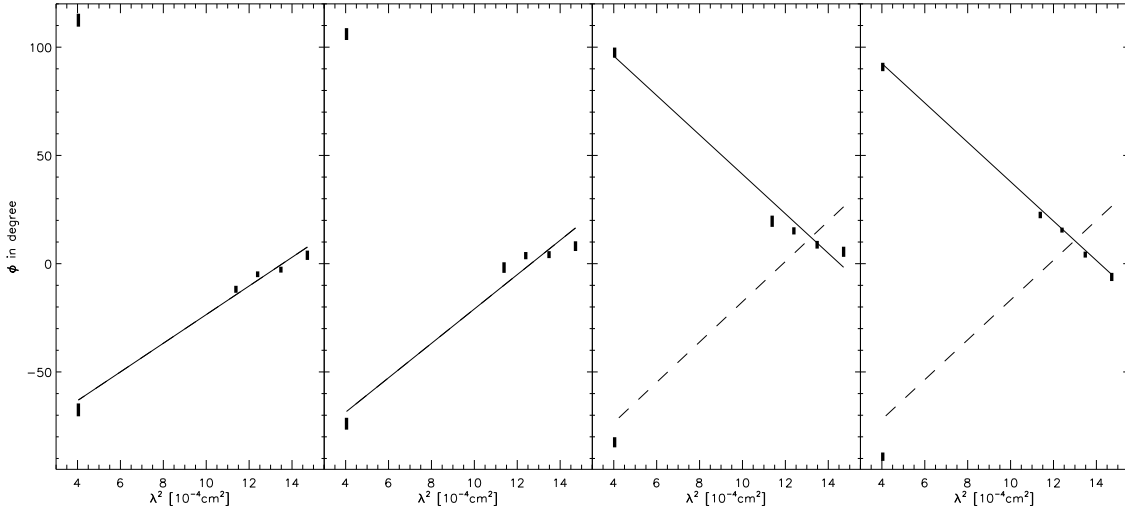


Figure 8. An example for individual RM fits across a typical RM jump observed in the RM maps of the south lobe of Hydra A. The solid line indicates the standard fit solution and the dashed one represents the *Pacman* solution. The error bars in these plots indicate the polarisation errors which were multiplied by 3. Note that this is an extreme example, where *Pacman* chooses a solution to the individual fits which has not the minimal χ^2 but the resulting RM value seems to fit better in the global RM distribution.

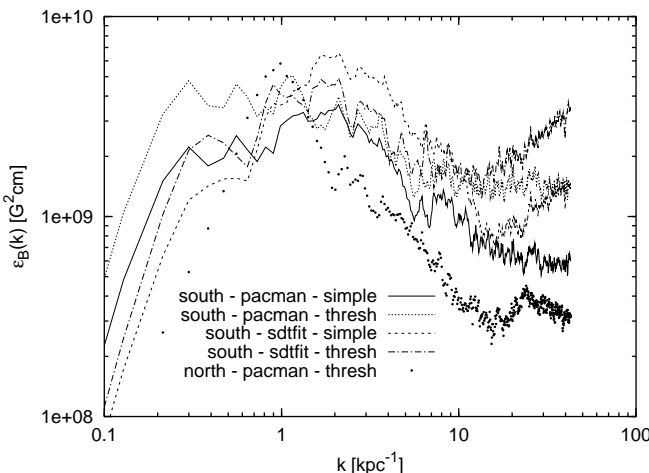


Figure 9. Various power spectra for the RM maps of the south lobe of the Hydra source are compared with the power spectrum of the north lobe calculated from the *Pacman* RM map ($k_{\min} = 5$, $\sigma_k^{\max} = 35^\circ$) employing a threshold weighting with $\sigma_0^{\text{RM}} = 50 \text{ rad m}^{-2}$ represented as filled circles.

the data at hand. *Pacman* has some resistance to pick this smallest χ^2 solution if it does not make sense in the context of neighbouring pixel information. As an example, we plotted individual RM fits which are typically observed across the RM jumps in Fig. 8. However as shown above, one has to consider that the measurement errors might be underestimated which gives much tighter constraints on the fit than it would otherwise be.

In order to investigate these maps further, we also calculated the threshold weighted ($\sigma_0^{\text{RM}} = 50 \text{ rad m}^{-2}$) and simple weighted power spectra from the *Pacman* and the standard fit RM maps of the south lobe and compared them to the one from the north lobe. The RM maps used for the comparison were all calculated employing $\sigma_k^{\max} = 35^\circ$ and $k_{\min} = f = 5$. The various power spectra are shown in Fig. 9. One can clearly see that the power spectra calcu-

lated for the south lobe lie well above the power spectra from the north lobe, which is represented as filled circles.

Concentrating on the comparison of the simple window weighted power spectra of the south lobe in Fig. 9 (solid line from *Pacman* RM map and dashed line from standard fit RM map) to the one of the north lobe, one finds that the power spectrum calculated from the *Pacman* RM map is closer to the one from the north lobe than the power spectrum derived from the standard fit RM map. This indicates that *Pacman* RM map might be the right solution to the RM determination problem for this part of the source. However, this difference vanishes if a different window weighting scheme is applied to the calculation of the power spectrum. This can be seen by comparing the threshold window weighted power spectra (dotted line for the power spectra of the *Pacman* RM map and dashed dotted line for the power spectra from the standard fit RM map) in Fig. 9. Since the choice of the window weighting scheme seems to have also an influence on the result the situation is still inconclusive.

An indication for the right solution of the $n\pi$ -ambiguity problem may be found in the application of our *gradient vector product statistic* \tilde{V} to the *Pacman* maps and the standard fit maps of the south lobe (as shown in Fig. 1). The calculations yielded a ratio $\tilde{V}_{\text{stdfit}}/\tilde{V}_{\text{pacman}} = 12$. This is a difference of one order of magnitude and represents a substantial decrease in correlated noise in the *Pacman* maps. The calculation of the normalised quantity yielded $V_{\text{stdfit}} = -0.69$ for the standard fit maps and $V_{\text{pacman}} = -0.47$ for the *Pacman* maps. This result strongly indicates that the *Pacman* map should be the preferred one.

The final answer to the question about the right solution of the RM distribution problem for the south lobe of Hydra A has to be postponed until observations of even higher sensitivity, higher spatial resolutions and preferably also at different frequencies are available.

4 CONCLUSIONS & LESSONS

We demonstrated the robustness of our *Pacman* algorithm which is especially useful for the calculation of RM and φ^0 maps of extended radio sources. It dramatically reduces $n\pi$ -artefacts in noisy regions and makes the unambiguous determination of RMs in these regions possible. Any statistical analysis of the RM maps will profit from this improvement.

In the course of this work the observational data taught us the following lessons:

(i) It is important to use all available information obtained by the observation. It seems especially desirable to have a good frequency coverage. The result is a smoother, less noisy map.

(ii) For the individual least-squares fits of the RM, it is advisable to use an error weighting scheme in order to reduce the noise.

(iii) Global algorithms are preferable, if reliable RM values are needed from low signal-to-noise regions at the edge of the source.

(iv) Sometimes it is necessary to test many values of the parameters RM^{\max} , σ_k^{\max} and σ_{\max}^{Δ} in order to investigate the influence on the resulting RM maps.

(v) One has to keep in mind that whichever RM map seems to be most believable, it might still contain artefacts. One should do a careful analysis by looking on individual RM pixel fits but one also should consider the global RM distribution. We presented the *gradient vector product statistic* \tilde{V} as a useful tool to estimate the level of reduction of cross-correlated noise in the calculated RM and φ^0 maps.

(vi) For the calculation of power spectra it is always preferable to use a window weighting scheme which has to be carefully selected.

(vii) Finally, under or overestimation of the measurement errors of polarisation angles (which will propagate through all calculations due to Gaussian error propagation) could influence the final results. We introduced an *S – statistic* in order to estimate if the errors are over or under estimated.

We conclude that the calculation of RM maps is a very difficult task requiring a critical view to the data and a careful noise analysis. However, we are confident that *Pacman* offers a good opportunity to calculate reliable RM maps and to understand the data and its limitations better.

ACKNOWLEDGEMENTS

We want to thank Federica Govoni and Greg Taylor for allowing us to use their data on Abell 2255 and Hydra to test the new algorithm. We like to thank Tracy Clarke, James Anderson and Phil Kronberg for useful comments on the manuscript. K. D. acknowledges support by a Marie Curie Fellowship of the European Community program "Human Potential" under contract number MCFI-2001-01227.

REFERENCES

Burns J. O., Roettiger K., Pinkney J., Perley R. A., Owen F. N., Voges W., 1995, ApJ, 446, 583

David L. P., Nulsen P. E. J., McNamara B. R., Forman W., Jones C., Ponman T., Robertson B., Wise M., 2001, ApJ, 557, 546

de Vaucouleurs G., de Vaucouleurs A., Corwin H. G., Buta R. J., Paturel G., Fouque P., 1991, Third Reference Catalogue of Bright Galaxies. Volume 1-3, XII, Springer-Verlag Berlin Heidelberg New York

Dolag K., Vogt C., Enßlin T. A., 2003, MNRAS, submitted

Enßlin T. A., Vogt C., 2003, A&A, 401, 835

Enßlin T. A., Vogt C., Clarke T. E., Taylor G. B., 2003, ApJ, 597, 870

Feretti L., Boehringer H., Giovannini G., Neumann D., 1997, A&A, 317, 432

Govoni F., Feretti L., Murgia M., Taylor G. B., Giovannini G., Dallacasa D., 2002, in ASP Conf. Series: Matter and Energy in Clusters of Galaxies Magnetic Fields in Clusters of Galaxies Obtained Through the Study of Faraday Rotation Measures. pp arXiv:astro-ph/0211292

Haves P., 1975, MNRAS, 173, 553

Ikebe Y., Makishima K., Ezawa H., Fukazawa Y., Hirayama M., Honda H., Ishisaki Y., Kikuchi K., Kubo H., Murakami T., Ohashi T., Takahashi T., Yamashita K., 1997, ApJ, 481, 660

Lane W. M., Clarke T. E., Taylor G. B., Perley R. A., Kassim N. E., 2003, pp arXiv:astro-ph/0309647

Peres C. B., Fabian A. C., Edge A. C., Allen S. W., Johnstone R. M., White D. A., 1998, MNRAS, 298, 416

Ruzmaikin A. A., Sokoloff D. D., 1979, A&A, 78, 1

Sarala S., Jain P., 2001, MNRAS, 328, 623

Struble M. F., Rood H. J., 1999, ApJS, 125, 35

Taylor G. B., Perley R. A., 1993, ApJ, 416, 554

Taylor G. B., Perley R. A., Inoue M., Kato T., Tabara H., Aizu K., 1990, ApJ, 360, 41

Vallée J. P., Kronberg P. P., 1975, A&A, 43, 233

Vogt C., Enßlin T. A., 2003, A&A, 412, 373